Electronic Supplementary Material (ESI) for Materials Horizons.

Supplementary Information

Enhancement of linearity range of stretchable ultrasensitive metal crack strain sensor via superaligned carbon nanotube-based strain engineering

Kang-Hyun Kim,[a] Soon Kyu Hong,[a] Sung-Hun Ha,[a] Luhe Li,[a] Hyung Woo Lee *[a,b] and Jong-Man Kim *[a,b]

[a] Department of Nano Fusion Technology and BK21 Plus Nano Convergence Technology Division, Pusan National University, Busan 46214, Republic of Korea.

[b] Department of Nanoenergy Engineering and Research Center for Energy Convergence Technology, Pusan National University, Busan 46214, Republic of Korea.

*Corresponding authors: hwl2010@pusan.ac.kr (H. W. Lee), jongkim@pusan.ac.kr (J. -M. Kim)

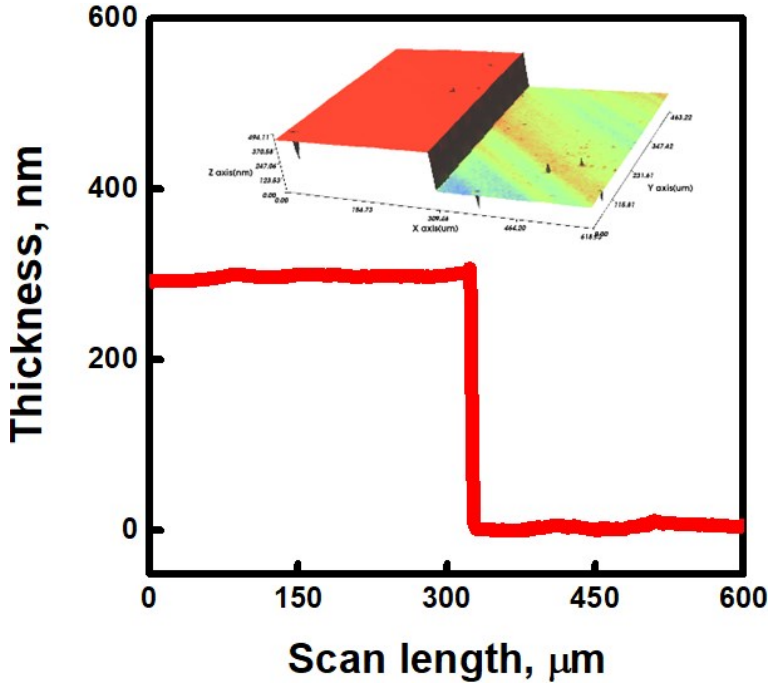

Fig. S1 Side profile of the Pt film patterned on a cleaned slide glass for thickness measurement, showing a typical film thickness of ≈300 nm (inset: corresponding 3D profile).

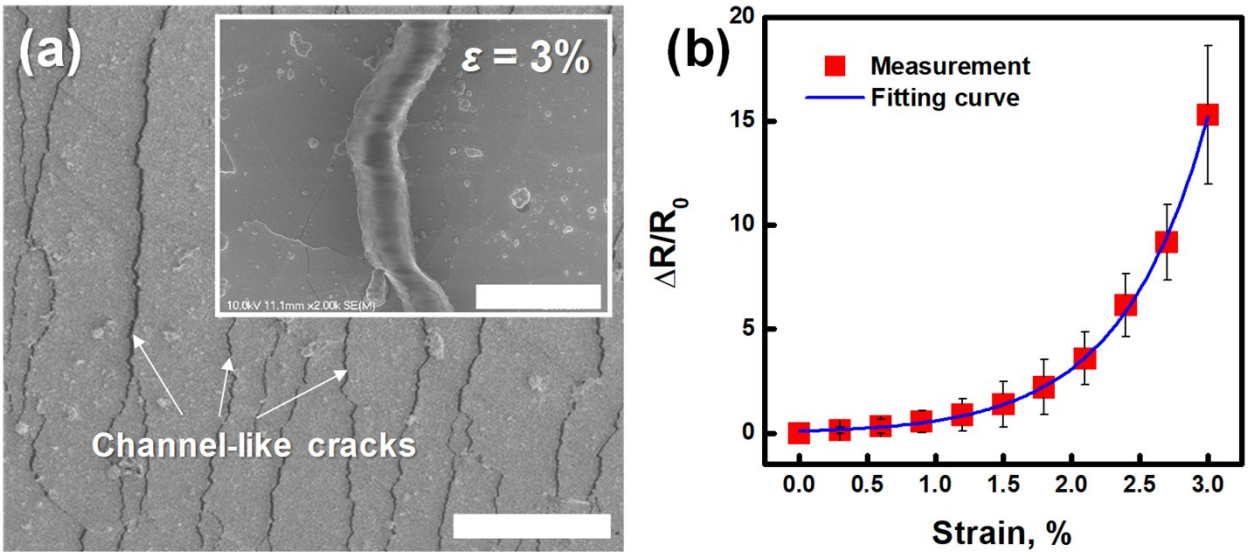

Fig. S2 Pt strain sensors. (a) Top-view SEM images of the fabricated device in the stretched (3%) state (scale bar: 500 μm) (inset: magnified SEM image (scale bar: 20 μm)) and (b) $\Delta R/R_0$ of the device as a function of applied strain.

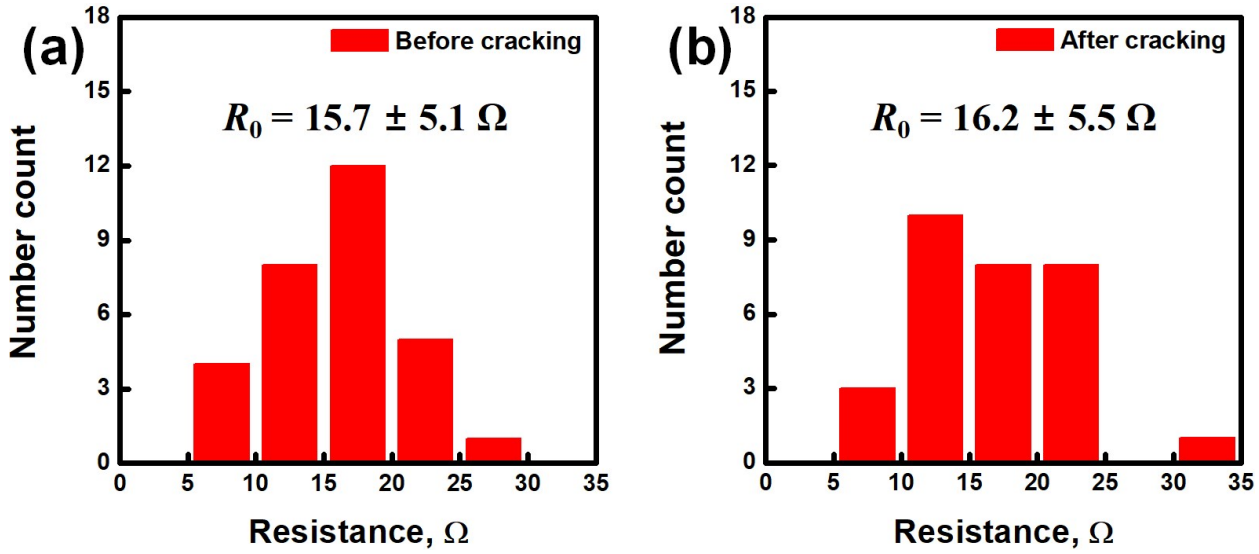

Fig. S3 Resistance distribution of the (a) as-prepared and (b) cracked PSAC films.

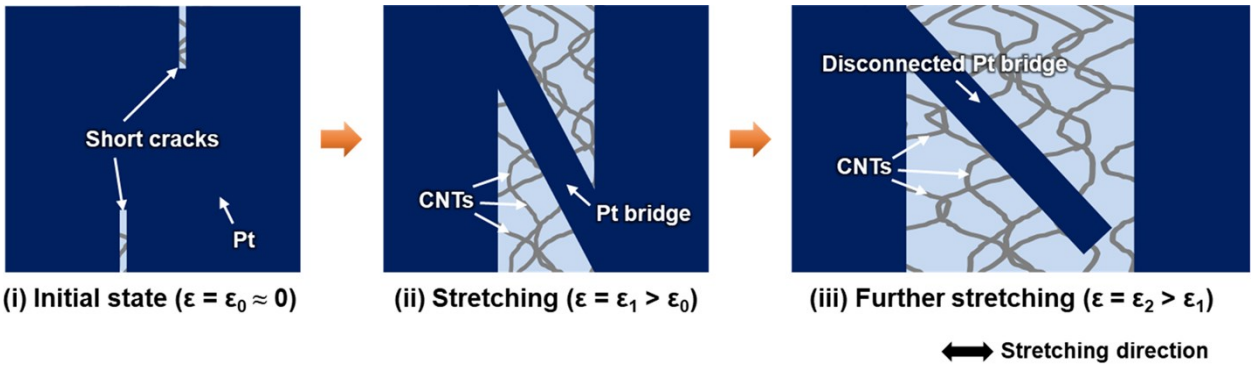

Fig. S4 Schematic illustration showing how the CNTs and Pt bridge are incorporated in the local area under high strains.

Fig. S4 illustrates the process showing how the CNTs and Pt bridge in the local area are incorporated at high strains. The short cracks randomly induced in the sensory film start to open with strain ($\varepsilon = \varepsilon_0 \approx 0$). As the crack gaps become wider with increased strain, a Pt bridge gradually elongates ($\varepsilon = \varepsilon_1 > \varepsilon_0$). In this strain range, the Pt bridge serves as a main conduction pathway because of its much higher electrical conductivity compared to that of the CNT network in the crack gaps. Meanwhile, even when the applied strain exceeds a critical strain at which the electrical pathway by the Pt bridge is broken ($\varepsilon = \varepsilon_2 > \varepsilon_1$), the CNT network can still maintain secondary current pathways in the sensory film.

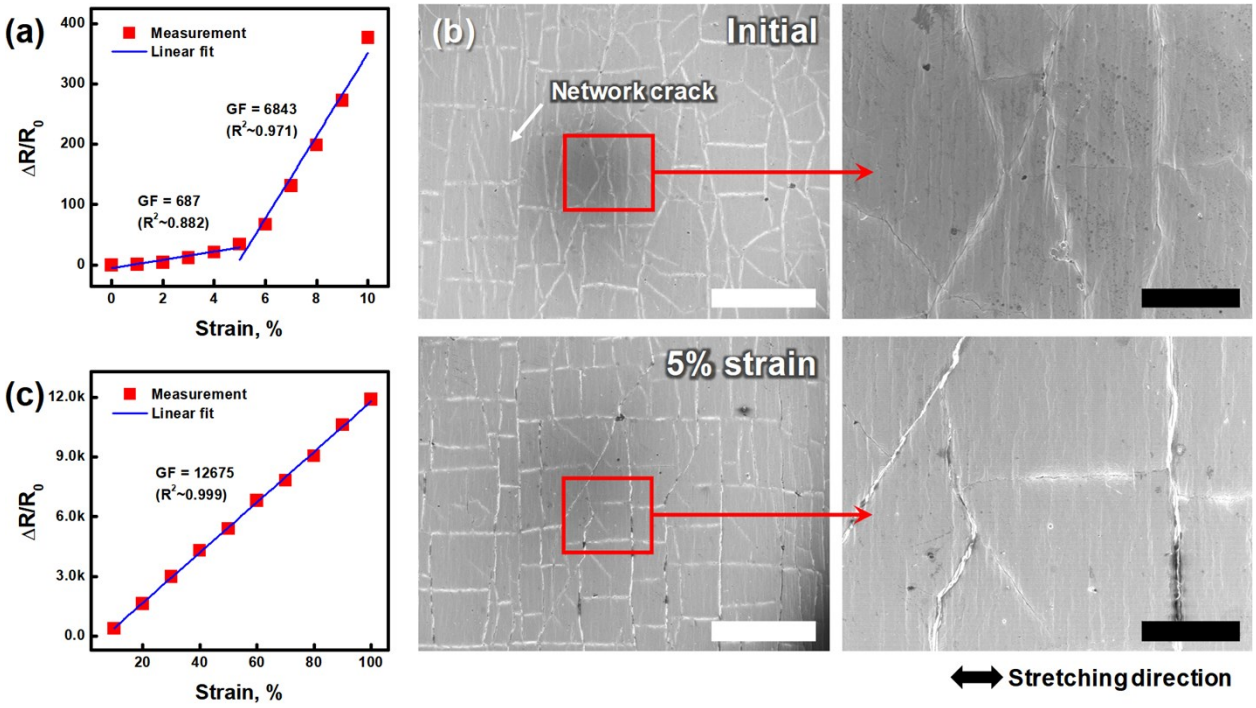

Fig. S5 Analysis of the response characteristics of the PSAC strain sensor at low strains. (a) $\Delta R/R_0$ curve of the device for up to 10% strain, (b) top-view SEM images of the device in the initial and 5%-stretched states (scale bars: 500 μm (white), 100 μm (black)), and (c) $\Delta R/R_0$ curve in the strain range of 10–100%.

To investigate the sensor response at low strains, the average ΔR/R0 values of the PSAC strain sensor are plotted for up to 10% strain, as shown in Fig. S5(a). The response curve could further be divided into two distinct strain regions with different slopes (i.e., GF ≈ 687 for 0–5% (R^2 ≈ 0.882) and GF ≈ 6843 for 5–10% (R^2 ≈ 0.971)). The relatively low slope of the $\Delta R/R_0$ curve at low strains might be because the cracking structure still remains robust enough that no significant change in resistance occurs in this strain regime owing to the network architecture. (Fig. S5(b)). Nevertheless, the GF value was as high as 687 up to 5% strain, suggesting that the PSAC strain sensor is capable of detecting even small strains in a precise manner.

Meanwhile, as expected, the highest GF and R^2 values could be obtained (i.e., GF ≈ 12675 and R^2 ≈ 0.999) for 10–100% strain, as shown in Fig. S5(c). However, no significant differences between the GF and R^2 values for 10–100% and 0–100% ranges were found although the response curve for 0–100% strain includes a slightly different slope at low strains (i.e., 0–10%).

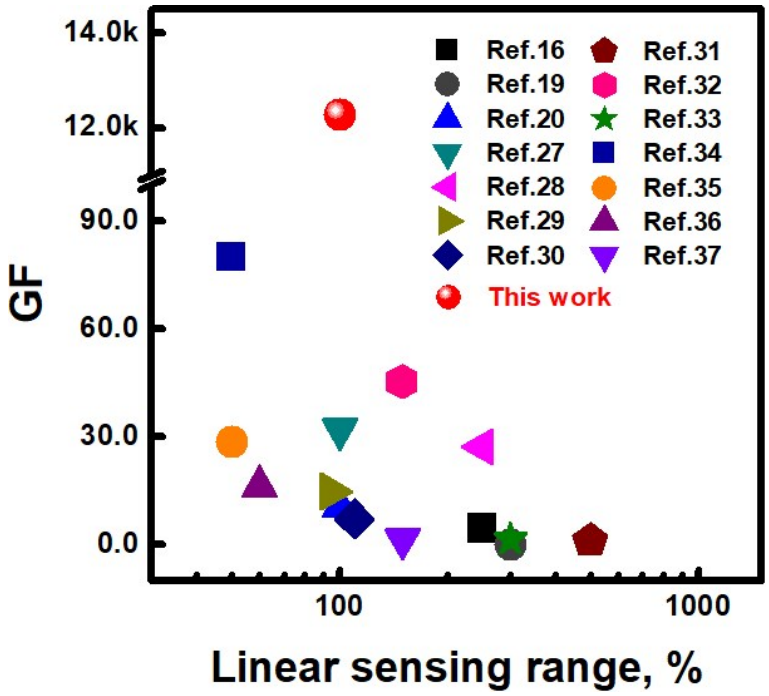

Fig. S6 Comparison of the gauge factor (GF) and linear sensing range of the PSAC strain sensors with those of other devices from literature having wide linearity up to ≈50% or higher strain.

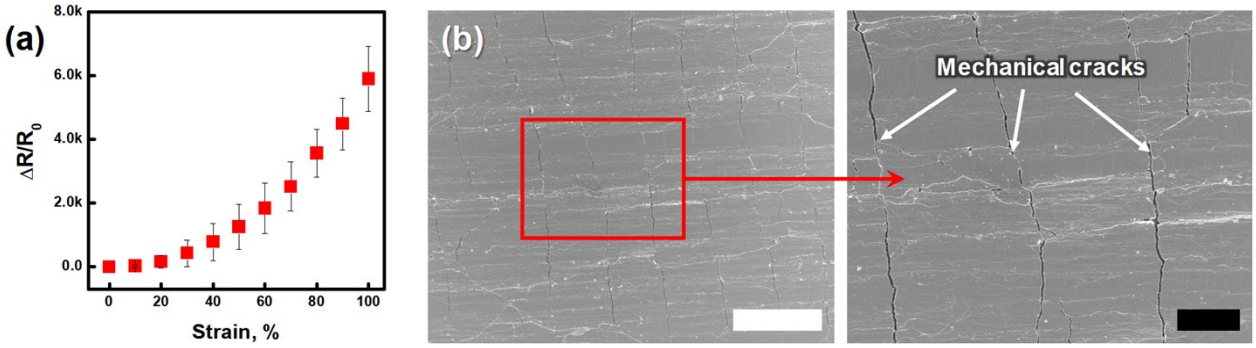

Fig. S7 PSAC-H strain sensor. (a) $\Delta R/R_0$ curve as a function of applied strain and (b) top-view SEM images of the device showing typical cracking structure (scale bars: 100 µm (white), 30 µm (black)).

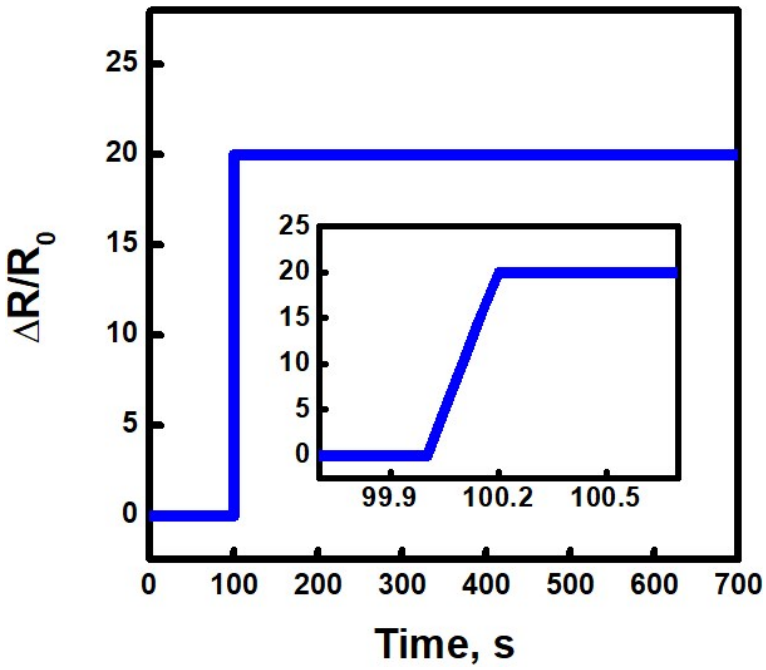

Fig. S8 Waveform of the strain signal applied to the PSAC strain sensor for characterizing the response speed (inset: magnified waveform).

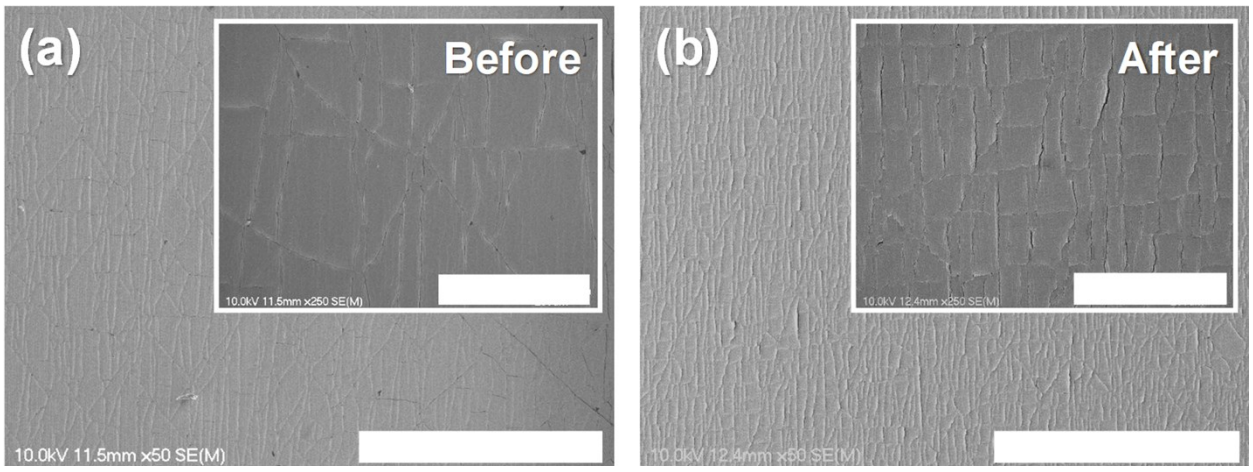

Fig. S9 Top-view SEM images of the PSAC strain sensor (a) before and (b) after the long-term stability test (2000 stretching/releasing cycles) (scale bars: 1 mm) (inset: magnified SEM images (scale bars: 200 μm)).

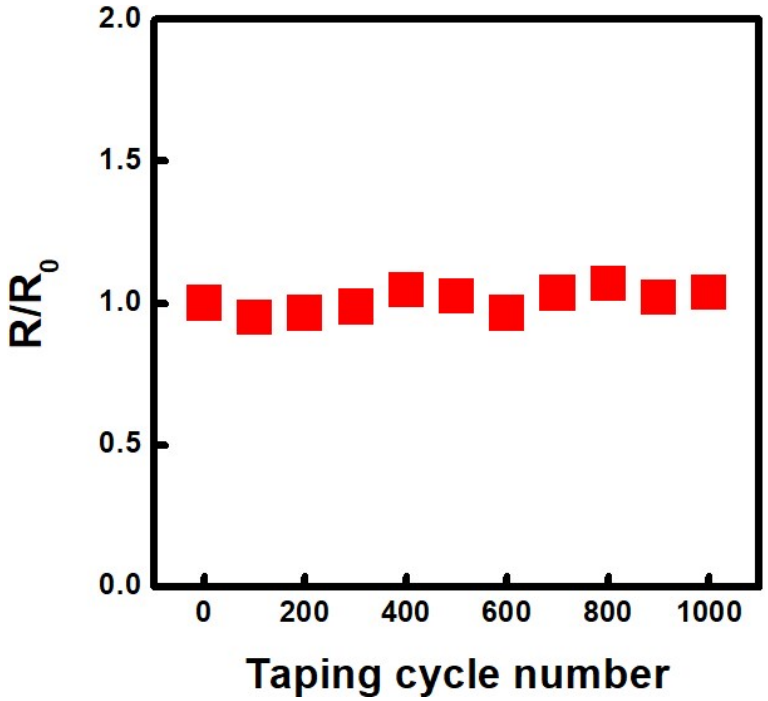

Fig. S10 Normalized resistance (R/R_0) of the PSAC strain sensor for repeated taping tests up to 1000 cycles.

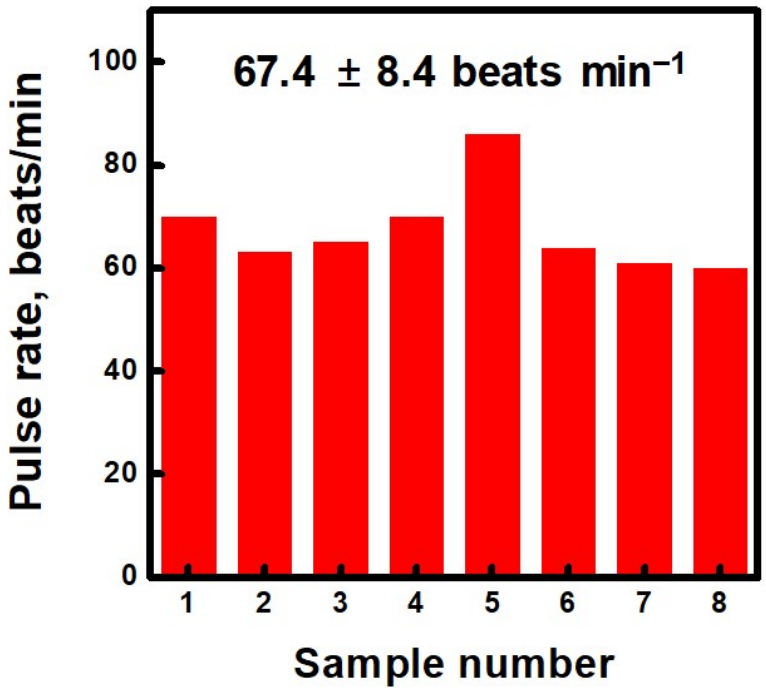

Fig. S11 Resting wrist pulse rates measured using eight individually prepared PSAC strain sensors.

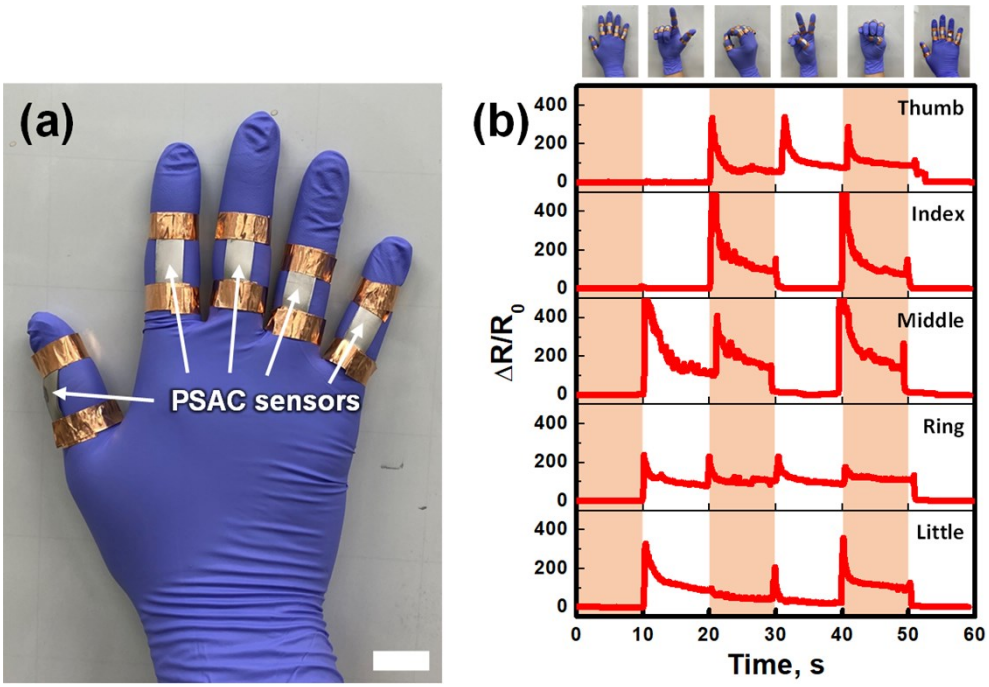

Fig. S12 Sensing glove. (a) Photograph of the sensing glove with five identical PSAC strain sensors attached to the finger joint regions (scale bar: 20 mm) and (b) $\Delta R/R_0$ curves of each sensor under various hand gestures.

The sensing glove was easily demonstrated by fixing five identical PSAC strain sensors onto the finger joint regions using a copper tape, as shown in Fig. S12(a). Fig. S12(b) shows the $\Delta R/R_0$ curves of each sensor as a function of time under the wearer's various hand gestures, which indicates that each sensor is capable of responding well to the real-time finger motions. This suggests that the stretchable PSAC sensors also show great potential as a practical strain-sensing solution in emerging applications such as robotics, virtual reality systems, and human-machine interfaces.